Micron 198 (2025) 103888

Contents lists available at ScienceDirect

Micron

journal homepage: www.elsevier.com/locate/micron

Liquid-cell annular dark-field scanning transmission electron microscopy imaging of single crystal samples on a low-index zone-axis incidence condition

Masaki Takeguchi [a,*], Jonathan Lueke [b], Matthew Reynolds [b], Baibing Zhao [c], Ayako Hashimoto [a,d]

[a] Research Center for Energy and Environmental Materials, National Institute for Materials Science, Tsukuba, Ibaraki, Japan
[b] Norcada, Edmonton, AB, Canada
[c] KITANO SEIKI Co., Ltd., Tokyo, Japan
[d] Graduate School of Science and Technology, University of Tsukuba, Tsukuba, Ibaraki, Japan

ARTICLE INFO

Keywords:
Liquid cell scanning transmission electron microscopy
Double-tilt
Focused ion beam
Zone-axis
Atomic-resolution
Channeling

ABSTRACT

In liquid cell (LC) annular dark-field scanning transmission electron microscopy (ADF-STEM), the spatial resolution is limited by the low ratio of signals from samples to background signals from the silicon nitride window membranes and liquid. We report the development of a double-tilt LC holder for atomic-resolution LC-ADF-STEM imaging of single-crystal samples under zone-axis incidence conditions. A $SrTiO_3$ <001> lamellar sample, approximately 100 nm thick, was prepared using the focused ion beam technique and transferred onto a silicon nitride window membrane of an LC chip via a glass probe pick-up method in air, which avoids Ga ion beam-induced damage to the window membrane. The sample adhered to the high-flatness window membrane and remained immobile, even when embedded in a water droplet. The sample and pure water were enclosed in an LC and observed under <001> zone-axis incidence conditions using aberration-corrected ADF-STEM. Electron channeling along the atomic columns enabled atomic-resolution LC-ADF-STEM imaging with high contrast, sufficiently overcoming background signals from window membranes and liquids. This high-contrast imaging technique could lower the probe current and is expected to mitigate electron-beam-induced radiolysis and minimize undesired sample damage, particularly under high-magnification imaging conditions.

1. Introduction

Liquid cell (LC) transmission electron microscopy (TEM) has become a powerful tool for characterizing samples in liquid environments through structural imaging, compositional analysis, and diffraction, similar to conventional TEM and scanning TEM (STEM) (Liao and Zheng, 2016; Pu et al., 2019; Prabhudev and Guay, 2020; Sung et al., 2022; Chen et al., 2023; Lv et al., 2025). LCs using silicon chips with thin yet robust silicon nitride (SiN_x) membrane windows formed by advanced microelectromechanical systems (MEMS) technology allow for nanoscale LC-(S)TEM experiments with high reproducibility (Williamson et al., 2003; Li et al., 2021; Koo et al., 2024). These systems are available as commercial products, enabling researchers to conduct LC-(S)TEM studies on the physical and chemical behaviors of various materials in liquids (Yang et al., 2023). Moreover, advancements in high-speed and sensitive cameras have increasingly facilitated the observation of the material dynamics in liquids with high temporal resolution. Nevertheless, SiN_x window membranes and thick liquids intrinsically limit the spatial resolution of this analysis, which remains an issue in LC-(S)TEM (De Jonge and Ross, 2011; De Jonge et al., 2019; Takeguchi et al., 2024).

The spatial resolution of imaging nanoparticles has been discussed by De Jonge and Ross (2011) and De Jonge et al. (2019), and it has been attributed to two main factors: elastic and inelastic scattering by the window membranes and liquids. Elastic scattering disturbs the amplitude and phase of the electron beams, whereas inelastic scattering causes chromatic aberrations. Another factor is resolution deterioration owing to the lowered sample/background signal-to-noise ratio (SNR). A thicker liquid and a smaller beam current result in a lower SNR, worsening the resolution. Thus, most high-resolution LC-(S)TEM studies have

* Correspondence to: Research Center for Energy and Environmental Materials, National Institute for Materials Science, Tsukuba, Ibaraki 305-0047, Japan.
E-mail address: TAKEGUCHI.Masaki@nims.go.jp (M. Takeguchi).

https://doi.org/10.1016/j.micron.2025.103888
Received 8 April 2025; Received in revised form 11 July 2025; Accepted 17 July 2025
Available online 17 July 2025

been conducted with 2D material-film LCs, where small liquid pockets are formed between the two films and enclose the samples and liquids. These pockets typically have a thickness of several tens of nanometers, providing a low background against the sample contrast. Graphene liquid cells (GLCs) are ideal and are widely used because of their extreme thinness, light elemental composition, mechanical flexibility, electrical and thermal conductivities, and chemical stability. Yuk et al. (2012) demonstrated colloidal Pt nanocrystal growth and dynamics in liquids using GLCs at an atomic resolution, followed by numerous studies on the atomic dynamics of various samples in different liquids (Wang et al., 2014; Ghodsi et al., 2019; Park et al., 2021). However, issues with GLCs and other 2D material-film LCs include the uncontrollability of the position and size of the liquid pockets and the difficulty of incorporating electrochemical electrodes. Thus far, researchers have chosen either Si-chip-based LCs or GLCs based on their specific purposes, such as morphological observations or the high-resolution imaging of samples. Efforts are ongoing to overcome these inherent disadvantages. Zhang et al. (2024) developed polymer film LCs equipped with electrodes to observe the atomic dynamics at electrified solid-liquid interfaces during Cu-catalyzed CO_2 electroreduction reactions. Using Si-chip-based LCs with coexisting gas and liquid phases is a straightforward method for increasing the sample SNR against the background of liquids. Techniques such as electron beam-induced gas bubble formation (Zhu et al., 2013), gas and liquid exchange via flow systems (Ummethala et al., 2025), and gradual liquid evaporation by partially opening the LC lid (Takeguchi et al., 2022) facilitate such liquid-gas coexistence in LCs, effectively reducing the liquid thickness. Controlling the bulge of the window also reduces liquid thickness (Wu et al., 2021). Serra-Maia et al. (2021) demonstrated the annular dark-field (ADF)-STEM crystal lattice imaging and electron energy loss spectroscopy (EELS) analysis of Pt nanopowders in liquids thinned by gas bubble formation. Atomic-resolution observations have primarily been conducted on nanoparticles and thin films, often utilizing phase-contrast TEM imaging techniques (Pivak et al., 2023; Rindle et al., 2025; Wei et al., 2024). ADF-STEM can obtain atomic-resolution images of nanoparticles when their orientation is coincident with the incident beam direction or when the nanoparticles are very small. There is growing demand for extending atomic-resolution LC-(S)TEM to single-crystal samples, akin to conventional vacuum environment electron microscopy studies. For example, the performance of electrocatalysts is influenced by the atomic structures of their facets (Kuo et al., 2015; Füngerlings et al., 2023; Wang et al., 2023). Therefore, atomistic imaging of the chemical reaction dynamics at the interfaces of single-crystal electrode facets and electrolyte liquids is expected to provide significant insights into their activation and degradation mechanisms. LC-ADF-STEM offers the potential to observe such electrode-liquid interfaces with atomic resolution. However, this has not yet been attempted on single-crystal electrode facets exposed to liquids because ADF-STEM requires zone-axis incidence conditions to resolve atomic structures, and currently available LC holders lack a double-tilt function to achieve this alignment.

The present study aims to develop a double-tilt LC holder and use it to observe single-crystal samples under zone-axis incidence conditions. This approach demonstrates that the electron-channeling effect can sufficiently enhance the contrast of the atomic columns to overcome the resolution limitations attributed to background signals from SiN_x window membranes and liquids. Single-crystal $SrTiO_3$ $<001>$ lamella samples are fabricated using the focused ion beam (FIB) technique. To avoid Ga ion beam-induced damage to the SiN_x windows during FIB-sample transfer, the samples are picked up and transferred in air using a glass probe under an optical microscope.

2. Theory and methods

2.1. Spatial resolution in LC-ADF-STEM

In this study, we focus on the LC-ADF-STEM mode. When a sample is attached to the internal surface of the top window of the LC, the STEM probe is scattered by the window and hits the sample. Under these conditions, the best spatial resolution is achieved because only the top window influences the probe quality.

The spatial resolution of LC-ADF-STEM is defined as (De Jonge and Ross, 2011; De Jonge et al.,2019; Takeguchi et al., 2024)

$$d_{xy}{}' = \sqrt{(d_{xy})^2 + (d_{blur})^2 + (d_{SNR})^2} \quad (1)$$

where d_{xy} is the resolution determined by electron optics, such as the gun brightness, spherical aberration, and aperture aberration (i.e., diffraction aberration). d_{blur} corresponds to probe broadening due to elastic scattering caused by the top window. Finally, d_{SNR} is the resolution, limited by the SNR derived from the sample/background signals given by De Jonge and Ross (2011), De Jonge et al. (2019)

$$SNR = \frac{N_{signal} - N_{bkg}}{\sqrt{N_{bkg}}} \quad (2)$$

where N_{signal} is the number of electrons scattered by the sample and collected with an ADF detector and N_{bkg} is the number of electrons contributing to the background. According to the Rose criteria, a sample in the matrix is visible when the SNR is greater than 3–5 (Rose, 1973; Reimer and Kohl, 2008). If the vertical length of the STEM probe is equivalent to or greater than the distance between the top and bottom windows (i.e., in the case of non-aberration- corrected STEM), N_{signal} and N_{bkg} are given by a simple 2D linear imaging model (Xin et al., 2008). However, when a probe with a large convergence angle is used in an aberration-corrected STEM instrument, the vertical length of the STEM probe is significantly shorter than the distance between the top and bottom windows. Thus, the 3D-STEM effect (i.e., the depth-sectioning effect) is remarkable; the sample contrast is enhanced relative to the background, and the SNR is improved. This mitigates resolution deterioration due to d_{SNR}, as reported elsewhere (Takeguchi et al., 2024).

2.2. Sample preparation and transfer, and ADF-STEM observations

A small piece of a single-crystal $SrTiO_3$(100) wafer (Crystal Base Co., Ltd., Japan) was coated with a 30 nm carbon layer using a carbon coater (JEC-560, JEOL Ltd., Japan) and then set in an FIB instrument (JIB-4000, JEOL Ltd., Japan) for standard FIB fabrication processes. After depositing a carbon protection layer on the targeted position, a lamella was thinned to around 1–2 μm along the $<001>$ direction and attached to a post of an Omniprobe® lift-out grid (EM Japan Co. Ltd., Japan) using epoxy glue. The TEM examination and gentle FIB thinning were repeated to further thin the target areas to approximately 100 nm, as shown in Fig. 1(a). Immediately after completing the FIB thinning processes, the lamella was cut off from the grid post, picked up using a glass probe under an optical microscope, as shown in Fig. 1(b), and transferred onto a SiN_x window membrane with a 50 μm × 250 μm area and 30 nm thickness (indicated by the black arrow) of an LC Si chip (Norcada, Canada), as shown in Fig. 1(c).

The LC is composed of a stack of two chips containing a SiN_x window and a Norcada proprietary reversible sealing system. One chip has an accommodating feature (groove) to house a gasket, a relatively large on-chip fluid reservoir and 200-nm-thick spacers as shown in Fig. 1(c). Another chip doesn't have such specific features. The 200-nm-thick spacers reduce the likelihood of membrane collapse during assembly.

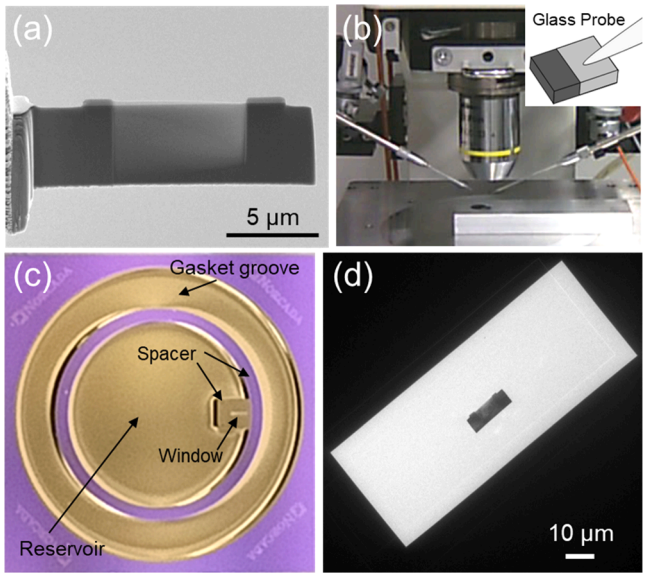

Fig. 1. (a) FIB-prepared $SrTiO_3$ <001> sample. (b) Glass probe sample pick-up system. (c) Top-view of a liquid cell chip with an on-chip fluidic chamber. (d) TEM image of the sample in (a) adhered on an LC chip window.

The above gasket reversibly seals between the two chips, creating a complete vacuum compatible seal between the two chips. The gasket receiving feature is made such that the two chips can still meet face to face, creating the tightest gap between the two chips. The window membrane and reservoir keep a balanced pressure between the two chips, allowing excess liquid and gas to move away from the membrane and the liquid to stay between the two membranes if the chips are well-hydrophilic. The SiN_x surface is usually hydrophilic in nature. The cleanliness of the surface is maintained as much as possible and not coated with photoresist when shipping. By hydrophilic treatment only, we can make the chip wet well to ensure that the liquid contained within the cell remains in the window area throughout the experiment. The two chip windows are slot-shaped and faced with orthogonal direction each other and the precision of the chip sizes are less than 50 μm so that a square viewing field of 50 μm× 50 μm could be obtained easily.

Our pick-up method is similar to the air-environment pick-up technique proposed by Lee et al. (2021), but we employed a glass probe instead of a biased tungsten probe. The FIB lamella pick-up system was supplied by JEOL, Ltd. (Japan). The glass probe was crafted from a glass tube with a diameter of 1 mm using a glass puller (P-10, Narishige Group, Japan) and a microforge (MF-900, Narishige Group, Japan). The glass probe effectively picked up the FIB-prepared semiconductor and insulator samples via electrostatic forces. This transfer process avoids Ga-ion irradiation-induced damage to the SiN_x window membrane without the need for complex dual-beam sample transfer procedures and specialized tools (Straubinge et al., 2016; Leonard and Hellmann, 2017). Fig. 1(d) shows a TEM image of the FIB-lamella adhering to the SiN_x window membrane. Selected-area diffraction patterns were also obtained to ensure that the misorientation angles were within the maximum tilting angle of the double-tilt LC holder. Following TEM checks, we confirmed that the chip remained immobile even when it was turned over and immersed in a water droplet.

The STEM instrument employed in the present study was a JEM-ARM200F (JEOL Ltd., Japan) equipped with a Schottky field-emission gun, double-aberration correctors, and an EELS device (Enfinium, Gatan Inc., USA) operated at 200 kV.

2.3. Double-tilt LC holder

Figs. 2(a) and 2(b) show a schematic cross-section and a photograph of the newly developed double-tilt LC holder, respectively. When the holder was inserted into the TEM sample chamber, the configuration of the two LC chips was flipped upside down, as shown in Fig. 2, and the FIB sample was positioned just below the top window membrane. We modified the JEOL double-tilt heating holder by replacing the original tiltable furnace holder with a tiltable LC holder. A Y-tilting rod was driven in the forward and backward directions using a JEOL TEM goniometer control console. It rotates an L-shaped transmission device connected to a spring, enabling the tilting of the LC holder component supported by the Y-axis pins. The maximum Y-tilting angle of the LC holder part for the gap of an HRP-type polepiece of the JEM-ARM200F was ± 8°, with a margin of several degrees.

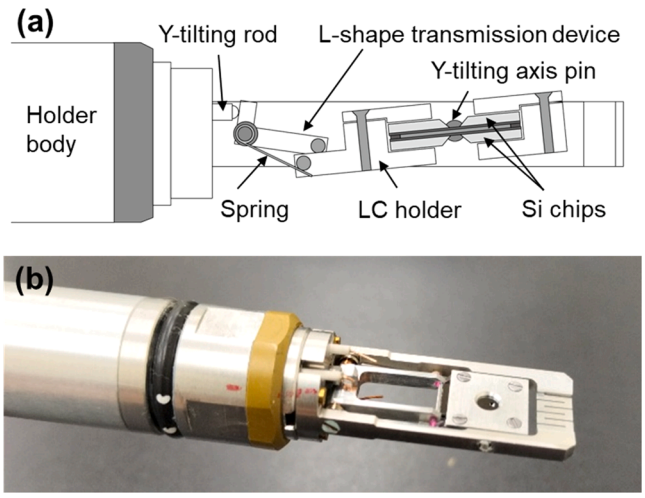

Fig. 2. (a) Schematic of the cross-section and (b) photo of the developed double-tilt LC holder.

2.4. ADF-STEM imaging using the electron channeling condition

In the present study, we used the electron channeling effect to enhance the contrast of the atomic columns in LC-ADF-STEM. When a single-crystal sample is aligned with the major zone axis, incident electrons are channeled along the atomic columns. This phenomenon occurs because negatively charged electrons are attracted to positively charged nuclei, confining them to narrow channels as they propagate through the crystal (Kirkland, 2005). Consequently, electron channeling increases the signal intensity of the atomic columns and extends the effective depth of fields in the ADF-STEM images. The intensity in ADF-STEM images is proportional to $tZ\alpha$ (t: thickness; Z: atomic number; α:1.5–2) (Kirkland, 2010; Tanaka, 2014); however, electron channeling modulates the atomic column intensity. It should be noted that electron propagation may exhibit probe intensity oscillations depending on the crystal structure and incident beam parameters.

We present an example of the crystal samples observed using ADF-STEM with intentional adjustments of the zone-axis conditions. Fig. 3 displays the ADF-STEM images of the FIB-prepared $SrTiO_3$ <001> sample, distinct from the sample shown in Fig. 1, captured in vacuum under on- and off-axis conditions. The right-hand side of the sample was in vacuum, and the thickness of the sample increased from the edge toward the left-hand side. The atomic columns are clearly visible in Fig. 3(a), but appear faint in Fig. 3(b). The line profiles along the yellow lines in these figures are presented in Fig. 3(c), illustrating that the image intensity of the atomic columns increases as the sample becomes thicker. Notably, the atomic column intensity in Fig. 3(a) was more than double that in Fig. 3(b), emphasizing the significance of the zone-axis alignment.

Another example involves a sample orientation accidentally aligned on the zone axis, resulting in high-contrast ADF-STEM images of the

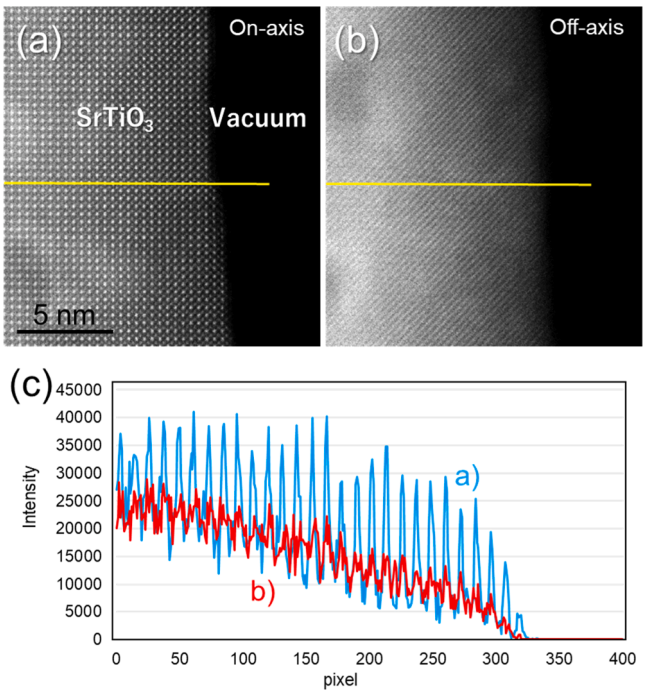

Fig. 3. (a, b) STEM images of an FIB-prepared $SrTiO_3$ <001> sample viewed at on- and off-axis conditions, respectively. (c) Line profiles colored blue and red obtained from the yellow lines shown in (a) and (b), respectively.

atomic columns. Fig. 4 presents the ADF-STEM images of the Pt nanowire networks within a Si chip cell, with 50-nm-thick windows filled with air at a dose rate of 3×10^5 e/nm^{2}s with a 28 mrad convergence angle and 52 pA probe current. The sample was prepared by sputter depositing Pt on the inner side of the SiNx window of the top chip at room temperature, as detailed previously (Takeguchi et al., 2023). The elapsed time is shown at the bottom-right of each image. The sequence of images captured continuous morphological changes of the Pt nanowire networks. By contrast, the same sample remained stable under vacuum conditions. During the morphological changes, one grain, indicated by the arrow in Fig. 4(a), gradually rotated. It then accidentally aligned its <110> orientation with the incident beam axis, revealing clear atomic structures, where the atomic columns appear as bright dots in Fig. 4(b). As the grains continued to rotate, the intensity of the atomic columns decreased, as shown in Fig. 4(c).

3. Results and discussion

Fig. 5(a) displays an FIB-prepared $SrTiO_3$ sample (differing from the sample shown in Fig. 1) attached to a post on an Omniprobe® grid, followed by repeated gentle FIB thinning and TEM checks. Fig. 5(b) shows a TEM image of the completed lamella with three distinct thicknesses. The lamella was then cut off from the post using the FIB and transferred onto the SiNx window membrane of the LC chip using a pick-up system, as illustrated in Fig. 5(c). After the chip was hydrophilized by 4 W ozone lamp illumination for 10 min, the chip was mounted on a double-tilt LC holder. Less than 0.1 μL of pure water was drop-casted onto the sample position and covered with another hydrophilized chip (the bottom window chip) before securing the LC with screws.

The sample was attached to a SiN_x window by electrostatic force in air. Attaching a flat sample to a high-flatness SiN_x window resulted in a more stable and secure attachment compared to using a wavy window. Interestingly, even when immersed in water, the samples remained stable and immobile. One possible explanation is the formation of a hydrated layer acting as an adhesive between the sample surface and the SiN_x window, although the exact mechanism remains unclear. The elucidation of the strong bonding observed between the samples and the window in water (liquid) will be investigated in future work.

Prior to LC-ADF-STEM observation, electron optics alignment, including tuning of the probe-forming lens aberration corrector, was performed using a holey carbon-film TEM microgrid mounted on a conventional single-tilt holder. This procedure aimed to minimize damage to the LC membrane and reduce radiolysis production from the liquid during tuning. Without altering the optimized STEM alignment, we swapped the conventional single-tilt holder for a double-tilt LC holder. Fig. 5(d) presents an LC-ADF-STEM image of the entire sample within the LC viewed through the LC windows. The $SrTiO_3$ sample was located on the internal surface of the top window of the LC. Note that this is reversed horizontally from Fig. 5(c) as the chip was flipped upside-down between Figs. 5(c) and 5(d). High-magnification images were obtained from the areas near the sample edge, as indicated by the yellow arrow in Fig. 5(d). A probe with a 21 mrad convergence angle and 15 pA current was employed. The X and Y tilt angles were adjusted by observing the Kikuchi pattern in a Ronchigram. Subsequently, the sample height was roughly set to the in-focus position using STEM images at a 512 × 512 pixel resolution. Magnification was increased to 8 million times with 1024 × 1024 pixels and a 5-μs pixel time, followed by fine adjustment of focus and astigmatism until atomic columns were clearly resolved. Magnification was then increased to 12 million times for acquiring high-resolution LC-ADF-STEM images at 1024 × 1024 pixels and a 10-μs pixel time. Occasionally, the acquisition area was selected slightly apart from the focal point to avoid the accumulation of

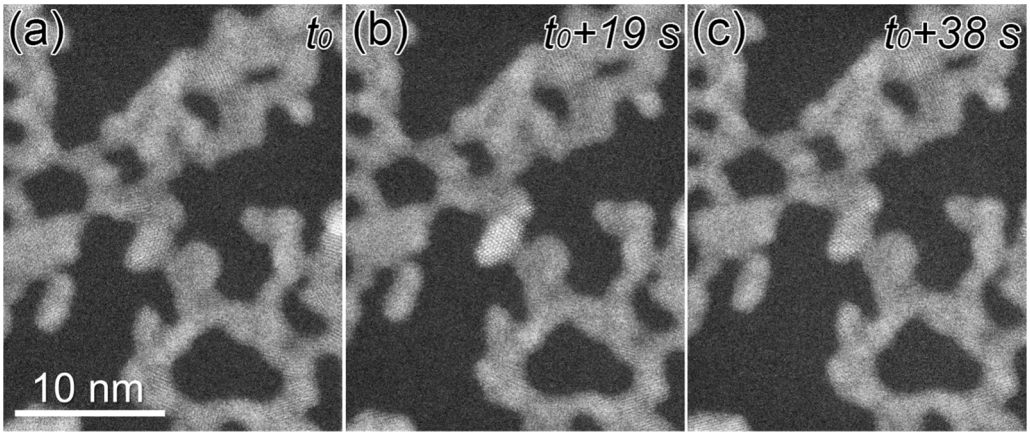

Fig. 4. ADF-STEM images of Pt nanowire networks in the Si chip cell with 50-nm-thick windows filled with air under a dose rate of 3×10^5 e/nm^{2}s, showing the morphological changes under the beam irradiation from (a) to (c). The elapsed time is displayed at the bottom right of each image.

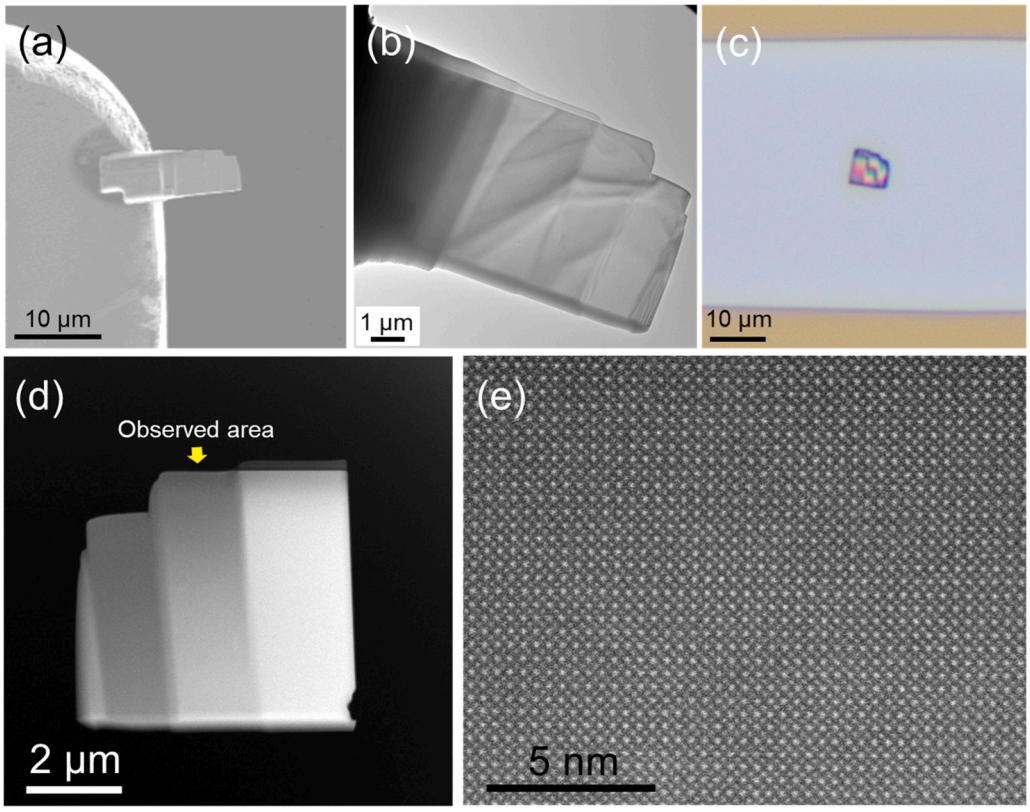

Fig. 5. (a) FIB-prepared $SrTiO_3$ <001> sample before gentle FIB thinning, (b) TEM image of the FIB sample lamella after the final thinning. Areas with three kinds of thicknesses (< 100 nm) exist. (c) Optical micrograph showing the sample on an LC chip window. (d) ADF-STEM image of the sample enclosed with pure water in the LC. (e) High-resolution ADF-STEM image of the area near the sample edge indicated by the yellow arrow after X and Y angle adjustment to the <001> zone axis.

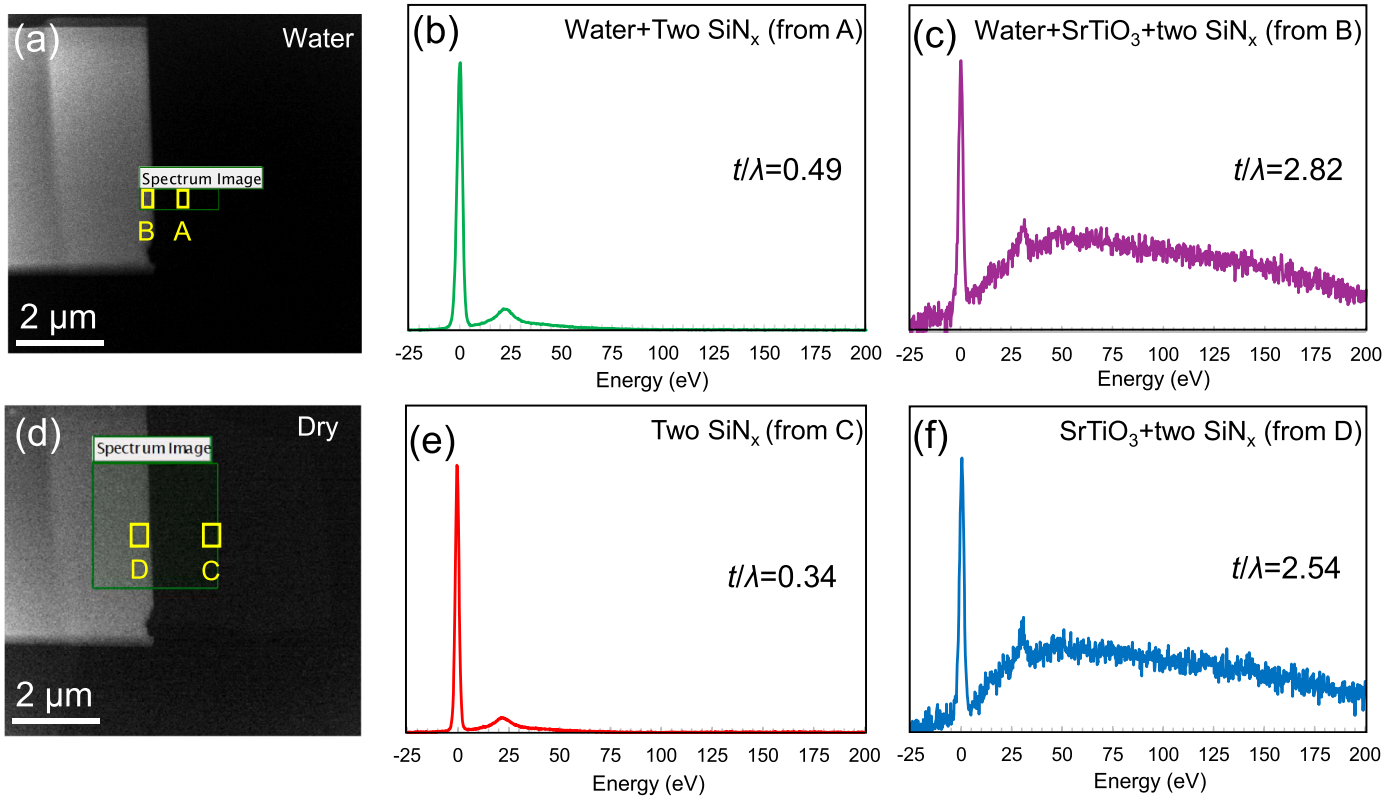

Fig. 6. (a) ADF-STEM image showing an area (green rectangle) for low- and high-loss energy-range EELS acquisition. (b) High and (c) low energy range EEL spectra taken from the SiN_x window area near the center of the green rectangle in (a). (d) Low energy range EEL spectrum taken from the SiN_x window area of the empty LC.

contaminants. The acquired LC-ADF-STEM image (Fig. 5(e)) clearly displays both Sr and Ti-O atomic columns.

To evaluate the thickness of the water layers on the $SrTiO_3$ sample and the SiN_x window, EELS was performed in the region highlighted by the green rectangle in Fig. 6(a). The water thickness was evaluated using the log-ratio method (Egerton, 1996). The relationship between the liquid thickness t_{liquid} and inelastic scattering mean free path (IMFP) λ_{liquid} is given by

$$t_{liquid}/\lambda_{liquid} = t_{total}/\lambda_{total} - t_{SiN}/\lambda_{SiN} \quad (3)$$

The IMFP λ value is given by

$$\lambda \approx 106F(E_0/E_m)/ln(2\beta E_0/E_m) \quad (4)$$

where F, E_0, E_m, and β are a relativistic factor (0.618 for $E_0 = 200$ keV), the incident energy, the mean energy loss, and the collection semi-angle, respectively. Using $E_m = 6.7$ for H_2O (Egerton, 1996) and $\beta = 17.6$ mrad, λ_{liquid} was calculated to be 281 nm. Here, it should be kept in mind that the accurate determination of the IMFP value of liquid water remains challenging. Recent detailed quantitative analyses using a nanochannel liquid cell with a well-defined liquid thickness suggested that the IMFP for liquid water is more than 50 % larger than the value given by Eq. (4) (Yesibolati et al., 2020).

Figs. 6(b) and 6(c) show EEL spectra obtained from regions on the SiN_x window (the area marked with a yellow rectangle labeled A in Fig. 6(a)) and the $SrTiO_3$ sample (the area marked with a yellow rectangle labeled B in Fig. 6(a)), respectively. The t/λ value calculated using Gatan Digital Micrograph® software (Gatan Inc., USA) is displayed for each region: $t/\lambda = 0.49$ and 2.82, respectively.

After the LC-STEM-EELS experiment, we opened the LC and separated the two chips. Part of the membrane of one chip was broken and lost during opening, but the $SrTiO_3$ sample survived and remained sandwiched between the two SiN_x membranes. Using this, as shown in Fig. 6(c), EEL spectra were obtained from the region highlighted by the green rectangle in the figure. Figs. 6(d) and 6(e) show results obtained from regions on the SiN_x window (the area marked with a yellow rectangle labeled C in Fig. 6(c)) and from the $SrTiO_3$ sample (the area marked with a yellow rectangle labeled D in Fig. 6(c)), respectively. The t/λ values for each were calculated to be 0.34 and 2.54, respectively, as displayed in the figure. By applying these values to Eq. (3) and using $\lambda_{liquid} = 281$ nm, the thicknesses of water on the $SrTiO_3$ sample and on the SiN_x region slightly away from the $SrTiO_3$ sample were evaluated to be 78.7 nm and 42.2 nm, respectively. In other words, the atomic-resolution image of the $SrTiO_3$ sample in Fig. 5(e) was obtained through approximately 78.7 nm of water and two SiN_x membranes, each 30 nm thick. The combined thickness of the observed $SrTiO_3$ region ($\approx$ 100 nm) and the water layer ($\approx$ 78.7 nm) is approximately 178.7 nm. Given that the spacer thickness of the chip was 200 nm and the $SrTiO_3$ sample was positioned at the center of the window (where the bulge was largest), it is reasonable to assume that an air layer exists between one membrane and the water-covered $SrTiO_3$ in Fig. 5.

Most high-resolution observations using Si-chip-based CLs have focused on nanoparticles and thin films, primarily utilizing bright-field (BF) TEM imaging techniques (Lv et al., 2025; Jin et al., 2019). Though TEM mode offers superior temporal resolution, BF signals for a single atom with atomic number Z vary roughly with $Z^{0.6}$ to $Z^{0.7}$ (Kirkland, 2010). By contrast, ADF signals depend on $Z^{1.5}$ to $Z^{1.7}$ (Kirkland, 2010). Therefore, LC-ADF-STEM is significantly more advantageous than LC-BF-(S)TEM for imaging samples containing heavier elements than the liquid (H_2O in the present work) and SiN_x in terms of the SNR, thus improving the d_{SNR} in Eq. (1). When this observation is extended from a single atom to a thick single crystal, the ADF intensity benefits from the increased number of atoms. To illustrate, comparing a single crystal sample with 100-nm thickness to a nanoparticle with 10-nm diameter, the former system includes 10 times more atoms contributing to the ADF intensity. Furthermore, aligning the incidence orientation of incident electrons on a low-index zone axis confines electrons within narrow atomic columns for penetration over distances exceeding several tens of nanometers, potentially greater than 100 nm, thereby enhancing the ADF intensity, as demonstrated in Fig. 3. Thus, applying LC-ADF-STEM to nearly 100-nm-thick single crystal samples under zone-axis incidence conditions facilitates atomic resolution imaging with high contrast, even within a liquid environment.

The proposed method lowered the probe current. In the present work, a probe with a current of 15 pA was employed, achieving a dose rate of 3.4×10^5 e/nm^{2}s at a magnification of 12 million times. Here, we roughly evaluate the SNR in Eq. (2) as follows: an accurate background intensity cannot be obtained because there is no area without a sample in Fig. 5(e). Therefore, the SNR was approximately calculated as $(N_{signal} - N_{bkg})/\sigma$, where σ is the standard deviation of a noise image obtained by subtracting a low-pass filtered image from the original one. The standard deviation for the noise image was calculated to be 9.9×10^4 using Gatan Digital Micrograph® software (Gatan Inc., USA). $N_{signal} - N_{bkg}$, obtained from a line profile along a Sr atomic column row in the central region of (e), was approximately 4.5×10^5. Thus, the SNR of the central region in (e) was evaluated to be approximately 4.5. According to the Rose criterion, Sr atomic columns are sufficiently visible when the SNR is greater than 3. This indicates the feasibility of further reducing the dose rate with a dose control system, such as a pulse illumination dose modulation system. Hence, LC-ADF-STEM observation of single crystal samples under zone-axis incidence conditions using a double-tilt LC holder facilitates atomistic investigations of material and liquid interactions at high magnifications. The SNR influencing to spatial resolution can be improved by reducing the scan speed (pixel time) if temporal resolution can be sacrificed. The balance between spatial and temporal resolutions must be considered depending on the phenomena targeted.

Furthermore, because the Si-chip-based LC can incorporate electrical stimulus functions, this technique allows the in situ observation of electrochemical reactions at solid-liquid interfaces with atomic resolution. This capability paves the way for deeper insights into material dynamics and interactions in various environments. Nevertheless, the influence of electron beams on samples placed in liquids may be still unavoidable. Such interactions induce sample charging and produce radiolysis products, promoting unexpected chemical reactions such as synthesis, dissolution, and growth (Hermannsdörfer et al., 2015). Therefore, to understand atomic dynamics at the solid-liquid interfaces, careful differentiation between intentional stimuli-induced and electron-beam-induced effects is required.

4. Conclusion

To achieve LC-ADF-STEM observations of an FIB-prepared single crystal sample under low-index zone-axis incidence conditions, two methodologies were developed. The first involves transferring the FIB-prepared samples onto the SiN_x window membrane of an LC using the glass probe pick-up method under an optical microscope in air. This approach effectively avoids Ga-ion beam-induced damage to the SiN_x window membrane. $SrTiO_3 < 001 >$ lamellar samples of approximately 100-nm thickness were used in this study. The samples were enclosed in an LC with pure water, with an estimated water thickness of approximately 48 nm, as determined using the EELS log-ratio method. However, the actual thickness may be larger, owing to the underestimated IMFP value for liquid water. The sample adhered to the high-flatness SiN_x window and remained stable, even when embedded in a water droplet. The second methodology involves the use of a double-tilt LC holder to orient the single crystal sample toward the desired low-index zone axis. The electron channeling effect enhanced the ratio of atomic column ADF signals to background signals from the SiN_x windows and liquid, effectively overcoming SNR-resolving limitations. Experiments demonstrated that the zone-axis incidence LC-ADF-STEM system enabled the high-contrast imaging of Sr and Ti-O atomic columns in FIB-

prepared single crystal samples in water. This high-contrast imaging technique is expected to facilitate a reduction in probe current, thus mitigating electron-beam-induced radiolysis and minimizing undesired sample damage, particularly under high-magnification imaging conditions. This technique will facilitate atomistic observations of reactions at solid-liquid interfaces. To improve upon this system, future studies should focus on developing strategies to distinguish between intentionally induced and electron-beam-induced effects and technologies to minimize radiolysis to negligible levels.

Funding

Part of this work was supported by GteX Program (Grant no. JPMJGX23H2, JST), the Innovative Science and Technology Initiative for Security (Grant no. JPJ004596, ATLA), Precursory Research for Embryonic Science and Technology (Grant no. JPMJPR17S7, JST), and KAKENHI (Grant no. 24K08252, JSPS).

CRediT authorship contribution statement

Ayako Hashimoto: Writing – review & editing. **Matthew Reynolds:** Methodology. **Baibing Zhao:** Methodology. **Masaki Takeguchi:** Writing – review & editing, Writing – original draft, Visualization, Validation, Project administration, Methodology, Investigation, Funding acquisition, Formal analysis, Data curation, Conceptualization. **Jonathan Lueke:** Methodology.

Declaration of Competing Interest

The authors declare that they have no known competing financial interests or personal relationships that could have appeared to influence the work reported in this paper.

Acknowledgements

We thank Ms. Y. Kobayashi and Ms. Y. Nakayama (National Institute for Materials Science) for fabricating the FIB samples and transferring them onto the LC chips. We thank Mr. H. Hosseinkhannazer (Norcada) for the helpful support regarding the LC chips and Mr. M. Kitano (KITANO SEIKI Co., Ltd.) for helping to manufacture a tiltable LC holder. We thank Editage (www.editage.jp) for English language editing. Part of this work was supported by the "Advanced Research Infrastructure for Materials and Nanotechnology in Japan (ARIM)" of the Ministry of Education, Culture, Sports, Science, and Technology (MEXT), Proposal nos. JPMXP1224NM5231, JPMXP1224NM5315, and JPMXP1224NM5318.

Data availability

Data will be made available on request.

References

Chen, Y., Yin, K., Xu, T., Guo, H., Sun, L., 2023. ACS Appl. Nano Mater. 6, 22545–22567. https://doi.org/10.1021/acsanm.3c03003.
De Jonge, N., Ross, F.M., 2011. Nat. Nanotechnol. 6, 695–704. https://doi.org/10.1038/nnano.2011.161.
De Jonge, N., Houben, L., Dunin-Borkowski, R.E., 2019. Nat. Rev. Matter 4, 61–78. https://doi.org/10.1038/s41578-018-0071-2.
Egerton, R.F., 1996. Electron Energy-Loss Spectroscopy in the Electron Microscope, Second Edition. Plenum Press, New York and London. https://doi.org/10.1007/978-1-4757-5099-7.
Füngerlings, A., Wohlgemuth, M., Antipin, D., Van der Minne, E., Kiens, E.M., Villalobos, J., Risch, M., Gunkel, F., Pentcheva, R., Baeumer, C., 2023. Nat. Commun. 14, 8284. https://doi.org/10.1038/s41467-023-43901-z.
Ghodsi, S.M., Megaridis, C.M., Shahbazian-Yassar, R., Shokuhfar, T., 2019. Small Methods 3, 1900026. https://doi.org/10.1002/smtd.201900026.
Hermannsdörfer, J., De Jonge, N., Verch, A., 2015. Chem. Commun. 51, 16393–16396. https://doi.org/10.1039/C5CC06812F.
Jin, B., Wang, Y., Liu, Z., France-Lanord, A., Grossman, J.C., Jin, C., Tang, R., 2019. Adv. Mater. 31, 1808225. https://doi.org/10.1002/adma.201808225.
Kirkland, E.J., 2005. Ultramicroscopy 102, 199–207. https://doi.org/10.1016/j.ultramic.2004.09.010.
Kirkland, E.J., 2010. Advanced Computing in Electron Microscopy, Second Edition. Springer, New York, NY. https://doi.org/10.1007/978-1-4419-6533-2.
Koo, K., Li, Z., Liu, Y., M. Ribet, S.M., Fu, X., Jia, Y., Chen, X., Shekhawat, G., Paul J.M. Smeets, P.J.M., Reis, R.D., Park, J., Yuk, J.M., Hu, X., Dravid, V.P., 2024. Sci. Adv. vol. 10, eadj6417. ⟨https://doi.org/10.1126/sciadv.adj6417⟩.
Kuo, C., Mosa, I.M., Thanneeru, S., Sharm, V., Zhan, L., Biswas, S., Aindow, M., Alpay, S. P., Rusling, J.F., Suib, S.L., He, Jie, 2015. Chem. Commun. 51, 5951–5954. https://doi.org/10.1039/C5CC01152C.
Lee, H., Okello, O.F.N., Kim, G., Song, K., Choi, S., 2021. Appl. Microsc. 51, 8. https://doi.org/10.1186/s42649-021-00057-8.
Leonard, D.N., Hellmann, R., 2017. J. Microsc. 265, 358. https://doi.org/10.1111/jmi.12509.
Li, X., Mitsuishi, K., Takeguchi, M., 2021. Microscopy 70, 327–332. https://doi.org/10.1093/jmicro/dfaa076.
Liao, H., Zheng, H., 2016. Annu. Rev. Phys. Chem. 67, 719–747. https://doi.org/10.1146/annurev-physchem-040215-112501.
Lv, H., Si, W., Sha, J., Chen, Yunfei, Zhang, Y., 2025. Next Nanotechnol. 7, 100115. https://doi.org/10.1016/j.nxnano.2024.100115.
Park, J., Koo, K., Noh, N., Chang, J.H., Cheong, J.Y., Dae, K.S., Park, J.S., Ji, S., Kim, I., Yuk, J.M., 2021. ACS Nano 15, 288–308. https://doi.org/10.1021/acsnano.0c10229.
Pivak, Y., Park, J., Basak, S., Eichel, R., Beker, A., Rozene, A., Garza, H., Sun, H., 2023. Microscopy 72, 520–524. https://doi.org/10.1093/jmicro/dfad023.
Prabhudev, S., Guay, D., 2020. Curr. Opin. Electrochem. 23, 114–122. https://doi.org/10.1016/j.coelec.2020.05.001.
Pu, S., Gong, C., Robertson, A.W., 2019. R. Soc. Open Sci. 7, 191204. https://doi.org/10.1098/rsos.191204.
Reimer, L., Kohl, L., 2008. Transmission Electron Microscopy. Springer, New York, New York. https://doi.org/10.1007/978-0-387-40093-8.
Rindle, O., Sixt, F., Spillane, L., Willinger, E., Gädt, T., 2025. Cem. Concr. Res. 193, 107853. https://doi.org/10.1016/j.cemconres.2025.107853.
Rose, A., 1973. Vision. Springer New York, New York. https://doi.org/10.1007/978-1-4684-2037-1.
Serra-Maia, R., Kumar, P., Meng, A.C., Foucher, A.C., Kang, Y., Karki, K., Jariwala, D., Stach, E.A., 2021. ACS Nano 15, 10228–10240. https://doi.org/10.1021/acsnano.1c02340.
Straubinge, R., Beyer, A., Volz, K., 2016. Microsc. Microanal. 22, 515. https://doi.org/10.1017/S1431927616000593.
Sung, J., Bae, Y., Park, H., Kang, S., Choi, B.K., Kim, J., Park, J., 2022. Annu. Rev. Chem. Biomol. Eng. 13, 167–191. https://doi.org/10.1149/1945-7111/acced4.
Takeguchi, M., Li, X., Mitsuishi, K., 2022. Jpn. J. Appl. Phys. 61 (SD), 1021. https://doi.org/10.35848/1347-4065/ac54f0.
Takeguchi, M., Takei, T., Mitsuishi, K., 2023. Nanomaterials 13, 2170. https://doi.org/10.3390/nano13152170.
Takeguchi, M., Hashimoto, A., Mitsuishi, K., 2024. Microscopy 73, 145–153. https://doi.org/10.1093/jmicro/dfae005.
Tanaka, N., 2014. Scanning Transmission Electron Microscopy of Nanomaterials: Basics of Imaging and Analysis. Imperial College Press, London. https://doi.org/10.1142/p807.
Ummethala, G., Jada, R., Dutta-Gupta, S., Park, J., Tavabi, A.H., Basak, S., Hooley, R., Sun, H., Garza, H.H.P., Eichel, R., Dunin-Borkowski, R.E., Malladi, S.R.K., 2025. Commun. Chem. 8, 8. https://doi.org/10.1038/s42004-025-01407-3.
Wang, C., Qiao, Q., Shokuhfar, T., Klie, R.F., 2014. Adv. Mater. 26, 3410–3414. https://doi.org/10.1002/smtd.201900026.
Wang, C., Zhang, Q., Yan, B., You, B., Zheng, J., Feng, L., Zhang, C., Jiang, S., Chen, W., He, S., 2023. Nano-Micro Lett. 15, 52. https://doi.org/10.1007/s40820-023-01024-6.
Wei, W., Sun, X., Sun, J., Hao, C., 2024. Molecules 29, 5342. https://doi.org/10.3390/molecules29225342.
Williamson, M.J., Tromp, R.M., Vereecken, P.M., Hull, R., Ross, F.M., 2003. Nat. Mater. 2, 532–536. https://doi.org/10.1038/nmat944.
Wu, H., Su, H., Joosten, R.R.M., Keizer, A.D.A., Van Hazendonk, L.S., Wirix, M.J.M., Patterson, J.P., Laven, J., De With, G., Friedrich, H., 2021. Small Methods 5, 2001287. https://doi.org/10.1002/smtd.202001287.
Xin, H.L., Intaraprasonk, V., Muller, D.A., 2008. Appl. Phys. Lett. 92, 013125. https://doi.org/10.1063/1.2828990.
Yang, R., Mei, L., Fan, Y., Zhang, Q., Liao, H., Yang, J., Li, J., Zeng, Z., 2023. Nat. Protoc. 18, 555–578. https://doi.org/10.1038/s41596-022-00762-y.
Yesibolati, M.N., Laganá, S., Kadkhodazadeh, S., Mikkelsen, E.K., Sun, H., Kasama, T., Hansen, O., Zaluzec, N.J., Mølhave, K., 2020. Nanoscale 12, 20649–20657. https://doi.org/10.1039/D0NR04352D.
Yuk, J., Park, J., Ercius, P., Kim, K., Hellebusch, D.J., Crommie, M.F., Lee, J., Zettl, A., Alivisatos, A.P., 2012. Science 336, 61–64. https://doi.org/10.1126/science.1217654.
Zhang, Q., Song, Z., Sun, X., Liu, Y., Wan, J., Betzler, S.B., Zheng, Q., Shangguan, J., Bustillo, K.C., Ercius, P., Narang, P., Huang, Y., Zheng, H., 2024. Nature 630, 643–647. https://doi.org/10.1038/s41586-024-07479-w.
Zhu, G., Jiang, Y., Huang, W., Zhang, H., Linc, F., Jin, C., 2013. Chem. Commun. 49, 10944–10946. https://doi.org/10.1039/C3CC46667A.